PAPER

Ni–CoSe2 heterojunction coated by N-doped carbon for modified separators of high-performance Li–sulfur batteries†

Kai Wang, [a] Haiqin Yang,[a] Ruiqiang Yan,*[a] Cairong Chen,[b] Chenglin Wu, [ac] Wei Chen, [a] Zhicai He, [a] Guobo Huang*[a] and Ling Chang*[acd]

Functional separators modified by transition metal compounds have been proven to be effective in suppressing the shuttle effect of polysulfides and accelerating sluggish electrode dynamics in lithium–sulfur batteries (LSBs). However, the behaviors of heterojunctions composed of transition metals and their compounds in LSBs are still rarely studied. Herein, we report a novel Ni–CoSe2 heterostructure coated with nitrogen-doped carbon. Compared to homogeneous cobalt diselenide, it exhibits much stronger adsorption and catalytic conversion abilities towards polysulfides. With the modified separators, the lithium–sulfur batteries exhibit significantly improved capacity retention and reduced polarization during cycling.

1 Introduction

Lithium–sulfur batteries employ high specific capacity sulfur (1672 mA h g^{-1}) as the cathode and metal lithium (3860 mA h g^{-1}) as the anode.[1–3] Therefore, their theoretical energy density far exceeds that of traditional lithium-ion battery systems, demonstrating extremely high application potential in future urban air traffic, high-altitude pseudo satellites, and other areas.[4,5] At the same time, sulfur materials also have advantages such as being abundant on earth, easy to process, and biocompatible.[6] However, the intermediate products generated by its reaction with lithium are soluble in the electrolyte and are prone to shuttle effects, leading to battery failure.[7,8] In addition, its lower electronic conductivity and poor reaction kinetics also limit the actual capacity of the material.[9,10]

One of the most effective methods to overcome the above problems is modifying commercial membranes with other functional materials.[11–13] The PP or PE separator in traditional lithium-ion batteries only serves the function of insulating and providing pathways for the transport of lithium ions. By modifying the surface of traditional separators with strong adsorption materials for polysulfides, the shuttle effect during the operation of lithium sulfur batteries can be effectively

suppressed, resulting in a significantly improved cycle life.[14,15] Similarly, decorating the membrane with conversion reaction catalysts is beneficial for improving electrode kinetics and reducing polarization, achieving better capacity utilization and rate performance.[16,17] According to this idea, various materials have been developed to modify separators of LSBs.[18,19] In the past decades, transition metal compounds (TMCs) have attracted a lot of research attention due to their excellent performance.[20,21] For example, polar metal oxides have isolated electron pairs in the O atom, leading to strong chemical adsorption of polysulfides.[22] Additionally, metal sulfides, metal selenides, metal nitrides, metal phosphides, and metal carbides have been demonstrated to be effective catalysts for the transformation of polysulfides.[23–27]

Heterostructure is composed of heterogeneous regions with different physical properties.[28] The mutual coupling between these heterogeneous regions can generate synergistic effects, thus possessing superior comprehensive performance.[29] In lithium–sulfur batteries, heterostructures can anchor lithium polysulfides and catalyze the acceleration of polysulfide conversion simultaneously, representing enormous application value.[30,31] According to this idea, a lot of heterostructures based on transition metal compounds have been designed, such as oxide–oxide, oxide–carbide, sulfide–nitride and so on.[32,33]

Herein, we have developed a novel transition metal-transition metal compound heterostructure (Ni–CoSe2@NC) by a simple route and applied it to construct functional modification layers for lithium sulfur battery separators. Compared to CoSe2, Ni–CoSe2 heterogeneous materials exhibit a stronger adsorption capacity for lithium polysulfides and catalytic ability for conversion reactions, thereby suppressing shuttle effects and reducing electrochemical polarization. Under the

aSchool of Pharmaceutical and Chemical Engineering, Taizhou University, Taizhou 318000, China

bTaizhou Prefectural Center for Disease Control and Prevention, Taizhou 318000, China

cTaizhou Biomedical and Chemistry Industry Institute, Jiaojiang, 318000, China

dDepartment of Chemistry, Zhejiang University, Hangzhou 310027, China

† Electronic supplementary information (ESI) available. See DOI: https://doi.org/10.1039/d4ra01660b

synergistic effect of the two, the battery exhibits significantly improved cycling and rate performance.

2 Experimental

2.1 Preparation of NiCo$_2$O$_4$@NC

Firstly, 0.001 mol NiSO$_4$·6H$_2$O and 0.002 mol CoSO$_4$·6H$_2$O were jointly dissolved in a 60 mL mixture of ethylene glycol and deionized water (volume ratio 1 : 1). Then, 30 mL 0.1 M Na$_2$C$_2$O$_4$ solution was poured into the above solution with continuous stirring. After stirred for 3 hours, the pink precipitate was collected by filtering. After drying overnight, 120 mg above precipitate and 240 mg dopamine hydrochloride were dispersed to 120 mL Tris-buffer solution by ultrasonic. After stirring for 24 h at room temperature away from light, the precursor was centrifuged and washed with ethanol and dried in an oven at 60 °C. To acquire NiCo$_2$O$_4$@NC composite, the dried sample was calcined under an Ar atmosphere at 500 °C for 2 h with a heating rate of 2 °C min^{-1}.

2.2 Synthesis of Ni–CoSe$_2$@NC composites

NiCo$_2$O$_4$@NC and selenium powder were mixed with the mass ratio of 1 : 5. The mixture was put into the porcelain boat and annealing in an Ar/H$_2$ (95/5, v/v) atmosphere at 350 °C for 2 h with a heating rate of 2 °C min^{-1}. The Ni–CoSe$_2$@NC was finally gained after cooling down to room temperature naturally.

2.3 Characterization

Scanning electron microscope (SEM) and transmission electron microscopy (TEM) were applied to observe the morphology and microstructure. X-ray diffraction (XRD) was used to characterize the crystal phase of the synthesized materials. Raman spectrum was employed to characterize the component of the samples. Element composition and surface chemical valence states were measured by X-ray photoelectron spectroscopy (XPS). The specific surface area and aperture distribution were tested by Brunauer–Emmett–Teller (BET). Ultraviolet-visible (UV) spectrophotometry was employed to analyze the adsorbent content of Li$_2$S$_6$ solution.

2.4 Electrochemical measurements

Coin cells were assembled in an Ar filled glovebox. The cathode was prepared according to the literature. Firstly, sulfur powder and carbon nanotubes were mixed and ground evenly with the weight ratio of 7 : 3. Then, the mixture was put into a sealed vessel and heated at 155 °C for 12 h. Then the sulfur/CNTs mixture, acetylene black and polyvinylidene fluoride (PVDF) were homogeneously mixed with a mass ratio of 8 : 1 : 1. Appropriate amount N-methyl-2-pyrrolidone (NMP) was added to the above composite to form a uniform slurry. Then, the slurry was coated onto the Al foil with a scraper and dried in an oven at 80 °C overnight. The dried electrode plate was punched into a disc with a diameter of 12 mm. The average S loading weight is 2.4 mg cm^{-2}. The modified separator was prepared by a similar way. The Ni–CoSe$_2$@NC, acetylene black and polyvinylidene fluoride (PVDF) were mixed and coating on

commercial PP membrane (Celgard 2400). Li foil was used as anode. The electrolyte was 1 M LiTFSI dissolved in a mixture of DOL and DME (v/v = 1 : 1). The cyclic voltammetry (CV) measurement was conducted on the CHI 760E between 1.7–2.8 V. Electrochemical impedance spectroscopy (EIS) was tested on Parstat 2273 electrochemical workstation (100 kHz–0.01 Hz). Galvanostatic charge–discharge measurements were carried out using a Neware battery test system (BTS 4000). Symmetric cells were assembled with a 0.2 M Li$_2$S$_6$ solution as electrolyte and tested at the scanning rate of 5 mV S^{-1} between −1 and 1 V. Li$_2$S nucleation tests were conducted with a 0.2 M Li$_2$S$_8$ solution at a constant voltage of 2.05 V.

3 Results and discussion

Fig. 1a shows the schematic diagram of the Ni–CoSe$_2$@NC functionalized PP separator and its application in lithium–sulfur batteries. The Ni–CoSe$_2$@NC composite is fabricated through a two-step solution reaction followed by a high-temperature selenization process. Subsequently, the modified PP separator was prepared by one-side casting with Ni–CoSe$_2$@NC slurry. In order to investigate the effects of the heterojunction composite on polysulfide intermediates, the coating layer is oriented toward the S cathode while PP faces the Li anode.
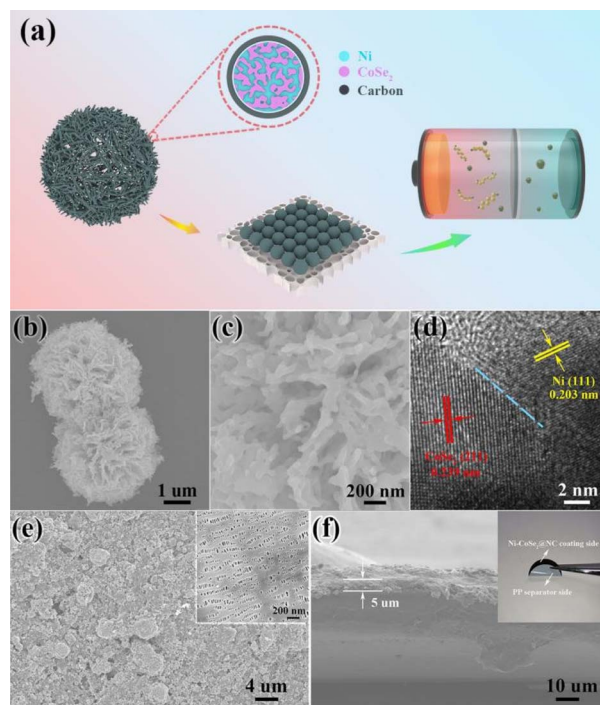

Fig. 1 (a) Schematic illustration of the structure of Ni–CoSe$_2$@NC functionalized PP separator and its application in lithium–sulfur batteries, (b and c) SEM and (d) TEM images of Ni–CoSe$_2$@NC heterojunction, (e) top view and (f) cross-sectional of Ni–CoSe$_2$@NC functionalized PP separator, inset in (e) is the top view of PP separator, inset in (f) is the optical photograph of Ni–CoSe$_2$@NC functionalized PP separator.
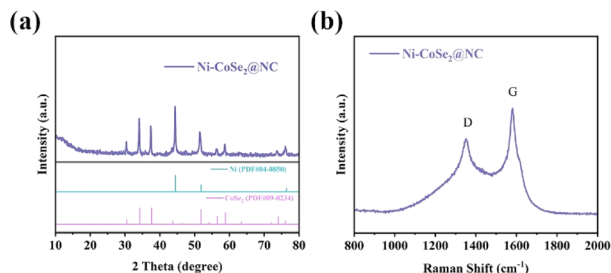
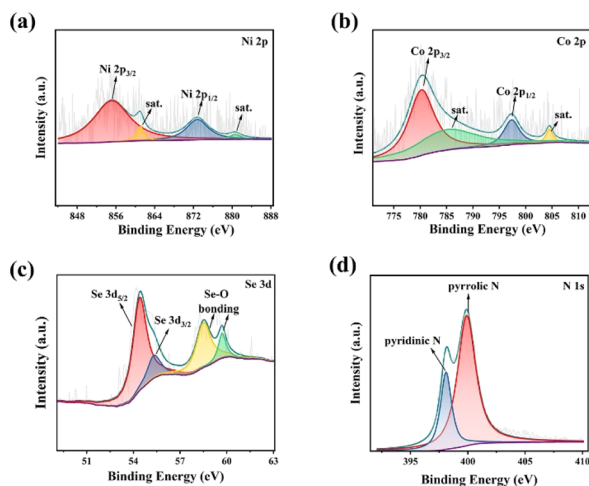**Fig. 2** (a) XRD pattern and (b) Raman spectrum of Ni–CoSe$_2$@NC composite.

Fig. 3 XPS spectra of (a) Ni 2p, (b) Co 2p, (c) Se 3d and (d) N 1s.

The morphology and microstructure of the Ni–CoSe$_2$@NC hybrid are observed by scanning electron microscopy (SEM) and transmission electron microscopy (TEM). The SEM image of Ni–CoSe$_2$@NC in Fig. 1b displays a microflower morphology with an average diameter of 4 μm. The magnified image in Fig. 1c shows that the microflower is composed of a large number of coralloid porous slices. The unique porous structure is beneficial for the uptake of electrolyte and adsorption of polysulfides.[34] Meanwhile, it can provide more transmission channels for Li$^+$. To confirm the porosity of the microflower, nitrogen adsorption–desorption testing was conducted. The typical type IV adsorption isotherms are shown in Fig. S1† demonstrates the mesoporous structure of the Ni–CoSe$_2$@NC composite.[35] The Brunauer–Emmett–Teller (BET) surface area is 132.4 m^2 g^{-1} and the average pore size is 6.8 nm. Fig. 1d is the HRTEM of the Ni–CoSe$_2$@NC heterojunction. The interplanar spacing of 0.203 nm is assigned to the (111) crystal plane of Ni (PDF #04-0850), while the lattice spacing of 0.239 nm can be ascribed to the (211) plane of CoSe$_2$ (PDF #09-0234). The amorphous area around Ni–CoSe$_2$ heterojunction is N-doped carbon derived from polydopamine. The EDS mapping in Fig. S2† shows different distributions of Ni and Co, which also proves the heterojunction structure. Fig. 1e is the top view of Ni–CoSe$_2$@NC functionalized PP membrane and the inset is the pristine separator. Clearly, the surface of PP separator was

coated by Ni–CoSe$_2$@NC composite uniformly. Fig. 1f is the cross-sectional image of the Ni–CoSe$_2$@NC coated PP separator and the thickness of functional layer is approximately 5 μm. The optical photograph in the inset of Fig. 1f presents the excellent flexibility and tightness of modified separator, which are favourable for maintaining good cycling stability.

XRD and Raman tests are employed to analyze the composition of final product. As shown in Fig. 2a, the XRD pattern suggests the presence of nickel metal and cobalt selenide in the final composite. The crystal plane information is consistent with the HRTEM result. Besides, there are no other crystal impurities. In order to investigate the evolution process of the composite, the crystal structure of intermediates was also tested. Fig. S3† reveals that the final Ni–CoSe$_2$@NC is derived from the selenization of Ni–CoSe$_2$@NC intermediate. Raman spectrum of Ni–CoSe$_2$@NC composite in Fig. 2b shows two distinct bands at Raman shift of 1351 and 1581 cm^{-1}, which are the characteristic peaks of carbon.[36] By combining all the analysis results, the composite is composed of metal Ni, CoSe$_2$ and amorphous carbon.

The surface chemical composition and valence state of Ni–CoSe$_2$@NC were characterized by X-ray photoelectron spectroscopy (XPS). The full spectrum in Fig. S4a† shows the existence of Se, C, N, O, Co and Ni elements. The high-resolution XPS spectrum in Fig. 3a displays the Ni 2p spectrum. The notable peaks at 855.1 and 872.8 eV are corresponded to Ni^0 2p$_{3/2}$ and Ni^0 2p$_{1/2}$, respectively. The peaks at 861.0 and 880.6 eV are the corresponding satellite peaks of Ni^0 2p.[37] In the Co 2p spectrum (Fig. 3b), the peaks located at 780.5 and 797.5 eV can be indexed to the Co^{2+} 2p$_{3/2}$ and Co^{2+} 2p$_{1/2}$, respectively. The two satellite peaks of the Co 2p are marked as "satellites".[38] Fig. 3c is the Se 3d spectrum. The two peaks at 54.5 and 55.4 eV can be assigned to Se 3d$_{5/2}$ and Se 3d$_{3/2}$, respectively. The peaks located at 58.6 and 59.8 eV can be attributed to the presence of Se–O bond, which may be caused by the absorbed oxygen on the surface of Se.[39] For the N 1s spectrum in Fig. 3d, two peaks with the binding energy of 398.1 and 399.9 eV are evidences of pyridinic N and pyrrolic N, respectively. N-doping is beneficial to enhance the chemisorption of polysulfide and promote the transformation of polysulfide,
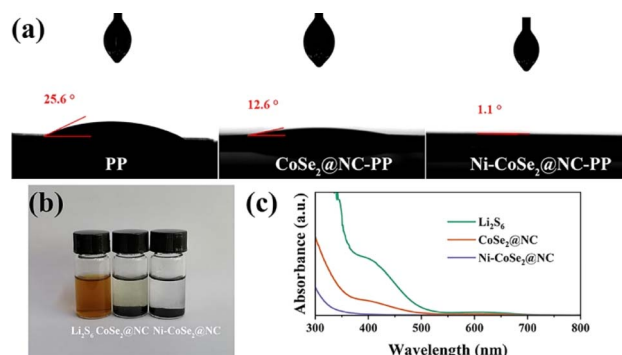

Fig. 4 (a) Contact angle tests of the pristine PP, modified CoSe$_2$@NC/PP and Ni–CoSe$_2$@NC/PP separators, (b) the optical image of adsorption experiments for the Li$_2$S$_6$ solution, (c) the corresponding UV-visible adsorption curves of above solutions.
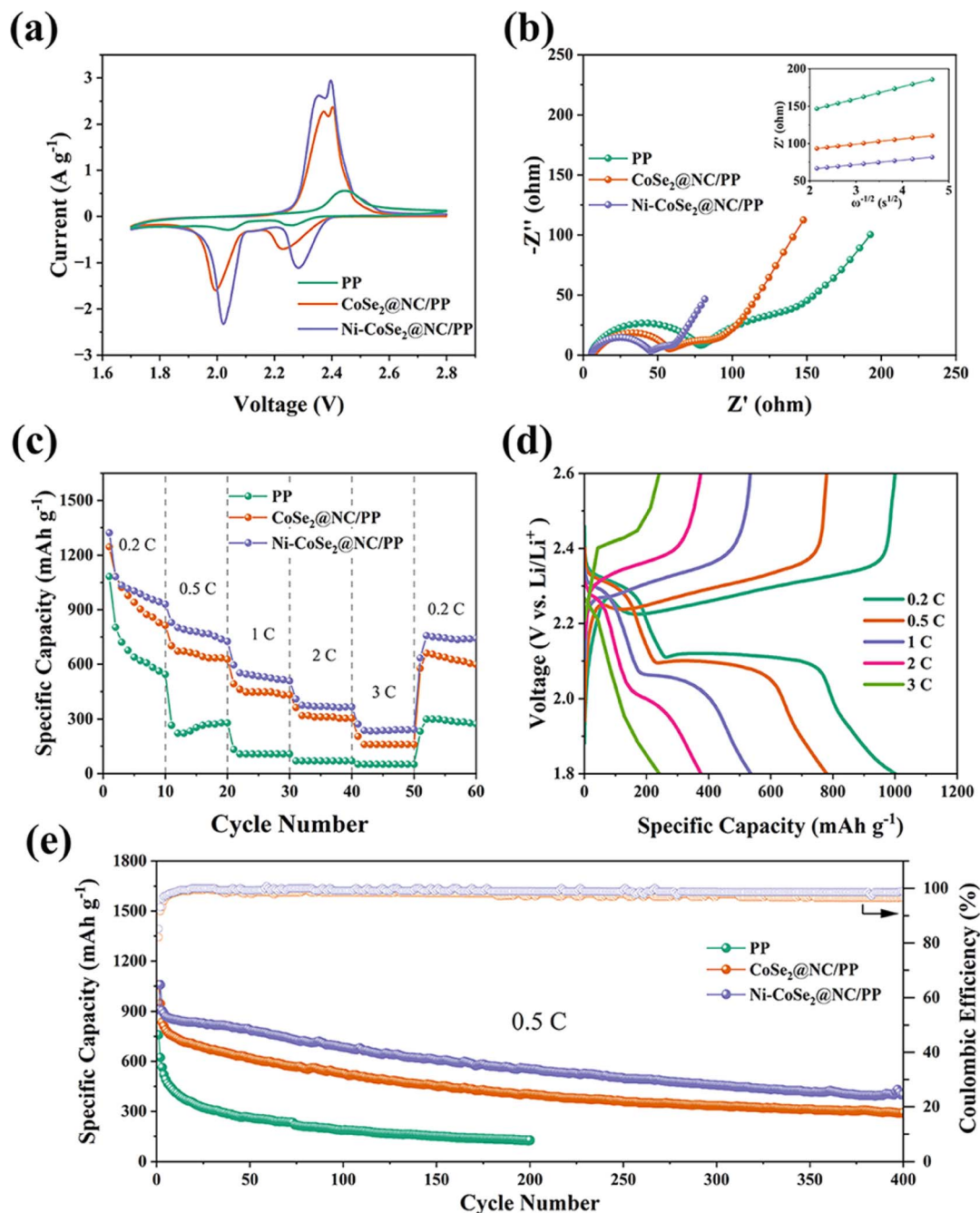
Fig. 5 (a) CV curves and (b) EIS of Li−S batteries assembled with the pristine PP, modified $CoSe_2@NC/PP$ and Ni−$CoSe_2@NC/PP$ separators, (c) the rate performance contrasts of various separators, (d) the charging−discharging profiles of the battery with Ni−$CoSe_2@NC/PP$ membrane, (e) the long cyclic performances of three different separators.

consequently inhibiting the shuttle effect effectively.[40] The C 1s spectrum is illustrated in Fig. S3b,† the signals centered at 284.5 and 285.5 eV are ascribed to the chemical bond of C–C and C–N, respectively.

To analyze the wettability of electrolyte on modified membranes, contact angle tests were conducted on the pristine, $CoSe_2@NC$ and Ni–$CoSe_2@NC$ modified separators respectively. As shown in Fig. 4a, all photographs were captured after adding electrolyte droplets for 1 second. Both modified

separators exhibited smaller contact angles than the pristine one, indicating better ion transfer efficiencies. The Ni–$CoSe_2@NC$ modified PP separator displays the best wettability of the electrolyte which can be ascribed to the polarity of the Ni–$CoSe_2$ heterojunction.[41] Fig. 4b shows the optical image of the adsorption experiments for the Li_2S_6 solution after 12 hours. As can be seen, the color of the Li_2S_6 solution remained dark brown while the solutions with adding $CoSe_2@NC$ and Ni–$CoSe_2@NC$ faded visibly. Corresponding UV-vis absorption

spectra in Fig. 4c shows a significant decrease in the absorption intensity of the solution containing Ni–CoSe$_2$@NC in the visible range, explaining the fading of the Li$_2$S$_6$ solution and testifying the strong polysulfide adsorbability of Ni–CoSe$_2$@NC.[42] Based on the Maxwell–Wagner–Sillars theory, the heterojunction with different dielectric properties and conductivities behaves an interfacial polarization derived from the charge redistribution. Comapred with CoSe$_2$, the different electronegativities and bonding states of the Ni and CoSe$_2$ heterojunction lead to an uneven distribution of space charge, which brings an electric dipole moment and larger polarity.[43,44]

The electrochemical performance of the modified separators is analyzed by assembling Li–S coin cells. Fig. 5a shows the cyclic voltammetry (CV) curves of various membranes recorded at 0.1 mV s^{-1}. As shown by the Ni–CoSe$_2$@NC/PP curve, there are two separate cathodic peaks corresponding to the conversion of sulfur to soluble intermediate polysulfides (Li$_2$S$_x$, $4 \leq x \leq 8$) and the final Li$_2$S/Li$_2$S$_2$ solid sequentially. Conversely, the anodic peaks around 2.35 and 2.39 V originate from the delithiation of low order lithium sulfides and high-order polysulfides respectively.[45] The curve of a similar shape implying the same reaction processes. The smaller voltage hysteresis in the Ni–CoSe$_2$@NC/PP curve between the oxidation and reduction peaks suggests lower polarization than CoSe$_2$@NC/PP. It demonstrates that the Ni–CoSe$_2$ heterojunction accelerates redox kinetics.[46] In addition, the change in peak current density of the pristine and modified separators indicates that Ni–CoSe$_2$@NC can significantly increase capacity utilization. Tafel plots fitted from the CV peaks are showed in Fig. S5.† As can be seen, the Ni–CoSe$_2$@NC modified separator displays the lowest slopes compared with other batteries both in the conversion of S$_8$ to final Li$_2$S and reversely. It proves that the Ni–CoSe$_2$@NC composite can promote both the formation and redox transformations of polysulfide effectively, resulting in an improved capacity and rate performance.[47] Electrochemical impedance spectroscopy is also tested and displayed in Fig. 5b. The Ni–CoSe$_2$@NC/PP battery has the smallest arc radius in the low frequency range and the highest straight line slope in the low frequency range, representing the best electrochemical kinetics.[48]

The galvanostat discharge performances with various separators are shown in Fig. 5c. As can be seen, the modified separators promote the specific capacities at all rates. Assembled with Ni–CoSe$_2$@NC/PP membrane, the battery exhibit a 930.3, 725.3, 507.7, 365.8 and 242.8 mA h g^{-1} at the rate of 0.2, 0.5, 1, 2 and 3C (1C = 1673 mA g^{-1}). When the current recovers to 0.2C, it also exhibits the highest capacity recovery (741.5 mA g^{-1}). To further study the superior catalytic function of Ni–CoSe$_2$@NC, CV curves of symmetrical batteries assembled with a Li$_2$S$_6$ electrolyte are compared in Fig. S6a.† Compared with blank and CoSe$_2$@NC electrodes, the CV curve of Ni–CoSe$_2$@NC composite exhibits a much higher current density, suggesting an accelerated reaction kinetics of polysulfides. In addition, the catalytic effect is further confirmed by the potentiostatic discharge experiments displayed in Fig. S6b.† Clearly, the Li$_2$S nucleation current of Ni–CoSe$_2$@NC composite deliver a earlier peak time and higher peak value, manifesting the better electrocatalytic activity of Ni–CoSe$_2$@NC heterostructures.[49] Fig. 5d shows the corresponding charging–discharging profiles of the battery with Ni–CoSe$_2$@NC/PP membrane. As current rates increase, capacities decline and differences between charging and discharging plateaus enlarge, which is a normal phenomenon of increased polarization. The cyclic performances are also compared (Fig. 5e). After 400 cycles of charging and discharging, the battery with Ni–CoSe$_2$@NC/PP still sustains a discharge capacity of 399.2 mA h g^{-1} while the CoSe$_2$@NC/PP only delivers 292.3 mA h g^{-1}. The highest capacity retention and coulombic efficiency indicate that the membrane modified with Ni–CoSe$_2$@NC can significantly ameliorate the cycling performance of lithium sulfur batteries. In further, XPS analysis of Ni–CoSe$_2$@NC composite after cycling is used to reveal its modification mechanism. As showed in Fig. S7,† the Ni 2p spectrum exhibits no obvious difference while the Co 2p peaks displays a negative shift, indicating the electrons in Li$_2$S$_6$ transferred to the Co atom.[50] Above results proved that CoSe$_2$ in the heterojunction plays a major role in the adsorption of polysulfides and the Ni component improves catalytic performance tremendously. In addition, we also test the cycling performance of batteries with the reversed separator, namely Ni–CoSe$_2$@NC modified side facing the lithium anode. As can be seen from the Fig. S8,† the cycling performance exhibited a fast decay of capacity at the beginning. It was even worse than that of batteries with commercial PP separator. This is mainly because the adsorption effect of the modification layer on lithium polysulfide enhances the shuttle of lithium polysulfide from the cathode to anode, leading to accelerated loss of active S in the cathode. The outstanding electrochemical performance aligns with the robust absorption of polysulfides and superior catalytic function of Ni–CoSe$_2$@NC composite.

4 Conclusions

In summary, a carbon coated Ni–CoSe$_2$ heterojunction with the morphology of coralloid microspheres has been fabricated successfully. After coupled with metal nickel, the composite displays better adsorbability of polysulfides than homogeneous cobalt diselenide. Additionally, it is capable of catalyzing conversion reactions and reducing polarization. Thanks to the synergistic effects of suppressing shuttle effects and accelerating reaction kinetics, the Ni–CoSe$_2$@NC modified PP separator exhibits significantly improved electrochemical performances. Such a transition metal compound junction design provides an alternative approach to realizing the practical application of LSBs in the future.

Author contributions

Kai Wang: conceptualization, methodology, validation, formal analysis, resources, writing – original draft preparation, project administration, funding acquisition. Haiqin Yang: revision. Ruiqiang Yan: software, validation, project administration. Cairong Chen: writing – review and editing. Chenglin Wu: validation, formal analysis. Wei Chen: validation, investigation, funding acquisition. Zhicai He: validation, resources. Guobo

Huang: validation, visualization, funding acquisition, project administration. Ling Chang: validation, writing – review and editing, project administration, revision.

Conflicts of interest

There are no conflicts to declare.

Acknowledgements

References

1 P. G. Bruce, S. A. Freunberger, L. J. Hardwick and J. M. Tarascon, *Nat. Mater.*, 2012, **11**, 19–29.

2 H. J. Peng, J. Q. Huang, X. B. Cheng and Q. Zhang, *Adv. Energy Mater.*, 2017, 1700260.

3 S. Bandyopadhyay and B. Nandan, *Mater. Today Energy*, 2023, **31**, 101201.

4 Z. Y. Jiang, S. L. Zhang, X. B. Dong, Z. L. Xu, M. T. Sarwar, C. Y. Yan, C. H. Yang, A. D. Tang and H. M. Yang, *New J. Chem.*, 2023, **47**, 4614–4618.

5 H. J. Zhao, N. P. Deng, J. Yan, W. M. Kang, J. G. Ju, Y. L. Ruan, X. Q. Wang, X. P. Zhuang, Q. X. Li and B. W. Cheng, *Chem. Eng. J.*, 2018, **347**, 343–365.

6 Y. B. Yang, S. X. Wang, L. T. Zhang, Y. F. Deng, H. Xu, X. S. Qin and G. H. Chen, *Chem. Eng. J.*, 2019, **369**, 77–86.

7 Q. Shu, *Mater. Res. Express*, 2019, **6**, 055508.

8 R. X. Zhu, S. Lin, J. F. Jiao, D. Y. Ma, Z. W. Cai, K. Hany, T. M. Hamouda and Y. R. Cai, *Ionics*, 2020, **26**, 2325–2334.

9 P. Zeng, C. Yuan, G. L. Liu, J. C. Gao, Y. G. Li and L. Zhang, *Chin. J. Catal.*, 2022, **43**, 2946–2965.

10 Z. H. Wei, Y. Q. Ren, J. Sokolowski, X. D. Zhu and G. Wu, *InfoMat*, 2020, **2**, 483–508.

11 S. Suriyakumar and A. M. Stephan, *ACS Appl. Energy Mater.*, 2020, **3**, 8095–8129.

12 B. Liu, X. M. Wu, S. Wang, Z. Tang, Q. L. Yang, G. H. Hu and C. X. Xiong, *Nanomaterials*, 2017, **7**, 196.

13 B. Li, Z. H. Sun, Y. Zhao and Z. Bakenov, *Polymers*, 2019, **11**, 1344.

14 N. P. Deng, W. M. Kang, Y. B. Liu, J. G. Ju, D. Y. Wu, L. Li, B. S. Hassan and B. W. Cheng, *J. Power Sources*, 2016, **331**, 132–155.

15 X. W. Yu, J. Joseph and A. Manthiram, *Mater. Horiz.*, 2016, **3**, 314–319.

16 Y. M. Kwon, J. Kim, K. Y. Cho and S. Yoon, *J. Energy Chem.*, 2021, **60**, 334–340.

17 Q. Q. Chen, J. L. Hu, Q. Xia, Y. P. Li, H. X. Zhong and L. Z. Zhang, *Mater. Today Commun.*, 2022, **31**, 103743.

18 S. W. Fan, G. D. Li, F. P. Cai and G. Yang, *Chem. Eur J.*, 2020, **26**, 8579–8587.

19 Y. Y. Xiang, Z. Wang, W. J. Qiu, Z. R. Guo, D. Liu, D. Y. Qu, Z. Z. Xie, H. L. Tang and J. S. Li, *J. Membr. Sci.*, 2018, **563**, 380–387.

20 J. J. Fu, Z. W. Shen, D. P. Cai, B. Fei, C. Q. Zhang, Y. G. Wang, Q. D. Chen and H. B. Zhan, *J. Mater. Chem. A*, 2022, **10**, 20525–20534.

21 X. Han, Y. Xu, X. Chen, Y.-C. Chen, N. Weadock, J. Wan, H. Zhu, Y. Liu, H. Li and G. Rubloff, *Nano Energy*, 2013, **2**, 1197–1206.

22 L. P. Wu, C. Y. Cai, X. Yu, Z. H. Chen, Y. X. Hu, F. Yu, S. J. Zhai, T. Mei, L. Yu and X. B. Wang, *ACS Appl. Mater. Interfaces*, 2022, **14**, 35894–35904.

23 X. F. Liu, D. Wang, X. Z. Yang, Z. Z. Zhao, H. Yang, M. Feng, W. Zhang and W. T. Zheng, *ACS Appl. Energy Mater.*, 2019, **2**, 1428–1435.

24 H. Wang, N. P. Deng, S. S. Wang, X. X. Wang, Y. N. Li, Q. Zeng, S. B. Luo, X. F. Cui, B. W. Cheng and W. M. Kang, *J. Mater. Chem. A*, 2022, **10**, 23433–23466.

25 G. Y. Xu, Q. B. Yan, P. Bai, H. Dou, P. Nie and X. G. Zhang, *ChemistrySelect*, 2019, **4**, 698–704.

26 Z. Song, X. Lu, X. Li, N. Jiang, Y. Huo, Q. Zheng and D. Lin, *J. Colloid Interface Sci.*, 2020, **575**, 220–230.

27 H. J. Peng, G. Zhang, X. Chen, Z. W. Zhang, W. T. Xu, J. Q. Huang and Q. Zhang, *Angew. Chem., Int. Ed.*, 2016, **55**, 12990–12995.

28 W. Chen, W. J. Zhang, K. Wang, L. Chang, R. Q. Yan, X. Q. Xiong, G. B. Huang and D. M. Han, *Langmuir*, 2023, **39**, 17830–17843.

29 W. Chen, R. Q. Yan, J. Q. Zhu, G. B. Huang and Z. Chen, *Appl. Surf. Sci.*, 2020, **504**, 144406.

30 T. Ren, X. Y. Wang, N. N. Wang, D. Huang, Y. Q. Zhu, P. K. Shen and J. L. Zhu, *J. Mater. Chem. A*, 2024, **12**, 5307–5318.

31 T. Wang, J. R. He, Z. Zhu, X. B. Cheng, J. Zhu, B. A. Lu and Y. P. Wu, *Adv. Mater.*, 2023, **47**, 35.

32 Y. Zhang, S. J. Wei, Z. P. Zhao, X. D. Pei, W. Zhao, J. B. Wang, X. Du and D. Li, *Small*, 2022, **18**, 2107258.

33 J. Balach, T. Jaumann, S. Mühlenhoff, J. Eckert and L. Giebeler, *Chem. Commun.*, 2016, **52**, 8134–8137.

34 Y. C. Mo, K. C. Yang, J. S. Lin, M. T. Liu, G. F. Ye and J. Yu, *J. Mater. Chem. A*, 2023, **11**, 6349–6360.

35 Z. W. Liang, C. Peng, J. D. Shen, J. J. Yuan, Y. Yang, D. F. Xue, M. Zhu and J. Liu, *Small*, 2023, 2309717.

36 X. Z. Fang, Y. Jiang, K. L. Zhang, G. Hu and W. W. Hu, *New J. Chem.*, 2021, **45**, 2361–2365.

37 L. Chang, Y. H. Zhou, S. A. Chen, K. Wang, Y. X. Jin, D. Chen, Y. Lin, W. Chen, R. Q. Yan, Z. C. He, G. B. Huang and H. Q. Tang, *J. Alloys Compd.*, 2023, **962**, 171187.

38 Y. X. Zhou, J. W. Zhang, C. Y. Zhao, T. Y. Shi, H. H. Yin, C. Q. Song, L. Qin, Z. L. Wang, H. B. Shao and K. Yu, *Dalton Trans.*, 2022, **51**, 14097–14106.

39 L. N. Zhang, T. S. Li, X. C. Zhang, Z. Y. Ma, Q. P. Zhou, Y. Liu, X. Y. Jiang, H. Y. Zhang, L. B. Ni and G. W. Diao, *J. Mater. Chem. A*, 2023, **11**, 3105–3117.

40 M. X. Wang, L. S. Fan, X. Sun, B. Guan, B. Jiang, X. Wu, D. Tian, K. N. Sun, Y. Qiu, X. J. Yin, Y. Zhang and N. Q. Zhang, *ACS Energy Lett.*, 2020, **5**, 3041–3050.

41 Y. Lei, Z. Y. Zhang, Z. Lin, S. Bhattacharjee and C. Chen, *Dalton Trans.*, 2024, **53**, 3985–3989.

42 H. Su, L. Q. Lu, M. Z. Yang, F. P. Cai, W. L. Liu, M. Li, X. Hu, M. M. Ren, X. Zhang and Z. Zhou, *Chem. Eng. J.*, 2022, **429**, 132167.

43 N. Zhai, J. Luo, J. Mei, Y. Wu, P. Shu, W. Yan and C. Li, *Adv. Funct. Mater.*, 2024, **34**, 2312237.

44 Z. Yang, T. Wang, J. Wang, Z. Luo, Q. Zhang and B. Zhang, *Carbon*, 2023, **201**, 491–503.

45 H. Shan, J. Qin, J. J. Wang, H. M. K. Sari, L. Lei, W. Xiao, W. B. Li, C. Xie, H. J. Yang, Y. Y. Luo, G. N. Zhang and X. F. Li, *Adv. Sci.*, 2022, **9**, 2200341.

46 L. Chang, Y. Lin, K. Wang, R. Q. Yan, W. Chen, Z. C. Zhao, Y. Y. P. Yang, G. B. Huang, W. Chen, J. Huang and Y. Z. Song, *RSC Adv.*, 2023, **13**, 440–447.

47 H. J. Kang, J. W. Park, H. J. Hwang, H. Kim, K. S. Jang, X. Ji, H. J. Kim, W. B. Im and Y. S. Jun, *Carbon Energy*, 2021, **3**, 976.

48 L. Chen, M. Shen, S. B. Ren, Y. X. Chen, W. Li and D. M. Han, *Nanoscale*, 2021, **20**, 9328–9338.

49 J. Liu, L. Yu, Q. Ran, X. Chen, X. Wang, X. He, H. Jin, T. Chen, J. S. Chen, D. Guo and S. Wang, *Small*, 2024, 2311750.

50 J. Wang, L. Zhou, D. Guo, X. Wang, G. Fang, X. Chen and S. Wang, *Small*, 2023, **19**, 2206926.